Supercapacitor and magnetic properties of NiO and manganese-doped NiO nanoparticles synthesized by chemical precipitation method

Nazir Ahmad Mala[1,*] (iD), Mohd Arif Dar[1], Mehraj ud Din Rather[2], Bilal Ahmad Reshi[3], S. Sivakumar[1,*], Khalid Mujasam Batoo[4], and Zubair Ahmad[5,*]

[1] *Department of Physics, Annamalai University, Annamalai Nagar, Tamilnadu 608002, India*

[2] *Department of Physics, Aligarh Muslim University, Aligarh 202002, India*

[3] *Department of Physics, Indian Institute of Technology, Guwahati, Assam 781039, India*

[4] *King Abdullah Institute for Nanotechnology, King Saud University, Riyadh 11451, Saudi Arabia*

[5] *School of Chemical Engineering, Yeungnam University, 280 Daehak-Ro, Gyeongsan, Gyeongbuk 38541, Republic of Korea*

ABSTRACT

In this research paper, pristine nickel oxide (NiO) and Mn-doped nickel oxide nanoparticles (NPs) were manufactured through the chemical precipitation method. The X-ray diffraction (XRD), Fourier transform infrared (FT-IR), UV–Visible diffuse reflectance spectroscopy, scanning electron microscopy/energy dispersive X-ray spectroscopy (SEM/EDX), transmission electron microscopy/selected area electron diffraction (TEM/SAED), vibrating sample magnetometer, and cyclic voltammetry were used to examine the pristine and Mn-doped NiO NPs. The XRD results confirmed that all the samples exhibit face-centered cubic structures with decreasing crystallite sizes. SEM and TEM studies show NPs have spherical morphology. The deviation in-between the high energy bandgap and optical absorption has been investigated in pristine and Mn-doped samples. The presence of a peak in the FT-IR spectra at 446 cm^{-1} confirmed the creation of the NiO phase. Hysteresis measurements show the exchange of weak ferromagnetic to superparamagnetism in the samples due to incorporation of Mn ions. It has been confirmed that the highest capacitance was measured at 555 F/g with a 10 mV/s scan rate for pristine NiO samples. In this research, the pristine NiO and Mn-doped NiO NPs can be used in data storage and supercapacitor applications.

Address correspondence to E-mail: nazirmala1990@gmail.com; girihari777@yahoo.com; zubair7157@yu.ac.kr

Springer

1 Introduction

In latest years, the exhaustion of fossil fuels has prompted the development of novel energy conversion and storage technologies. Supercapacitors serve an important role in electrochemical energy conversion and storage, owing to their high power density and elongated life cycle. Pseudocapacitance materials such as sulfides, metal oxides, and hydrides have got a lot of interest in the energy storage field. Due to their high specific capacitance, amorphous ruthenium oxides (RuO) are one of the greatest well-known materials for supercapacitors, but their exorbitant cost severely limits their use. Transition metal oxides (TMO) such as NiO, $C_{O3}O_4$, and MnO [1, 2] have been used to change RuO_2 since they are less costly and more eco-friendly materials with comparable electrochemical performance [2, 3]. Because of the vacancy at Ni^{2+} sites, NiO is essentially a p-type semiconductor material with a FCC structure. Below its (T_N = 523 K) Neel temperature, bulk NiO revealed the antiferromagnetic characterization [4, 5]. One of the best raw materials for applications involving pseudo-capacitor electrodes is NiO. Subsequently of its high theoretical specific capacity (Cs), superior thermal and chemical resilience, and small incidence [6]. Dopants can be inserted into the lattices of metal oxide to boost the electrode's electrochemical activity and discharge capacitance. The application of NiO is not limited to supercapacitors [7, 8] only but it extends to as a gas sensor [9, 10], catalyst [11], electrochromic film [12], and anode material for Li-ion batteries [6, 11].

Nanoparticles of NiO have been synthesized through various chemical route methods like the sol–gel method [13], solvothermal method [14], pulsed laser deposition approach [15, 16], the hydrothermal method [17], precipitation method [2], and chemical vapor deposition method [18]. Among these synthesis techniques, the precipitation method is one of the supreme methods for the preparation of NPs. The precipitation method is the low-cost and easiest method in which NPs are grown at low temperatures, with control over size as compared to other methods. Few studies have explored the magnetic characteristics of Mn-doped NiO NPs. However, the controversial reports are accessible for room temperature ferromagnetism (RTF) like that Hong et al. also show RTF in NiO thin films made with a pulsed laser deposition technique. Mn ions were found integrated into the NiO host [15]. According to Anandan et al., the photocatalytic efficiency of doped with Mn in NiO NPs was obtained using a simple precipitation technique. Their TEM and XRD data established that when Mn ions are combined with nickel ions, the size of the particles decreases [19]. According to Sanker et al., photocatalytic capabilities of Mn-doped NiO spherical NPs were synthesized utilizing an inexpensive sol–gel approach at ambient temperature. While the bandgap rises from 3.79 to 3.95 eV, the normal crystallographic size decreases from 35 to 30 nm [13]. However, Thangamani et al. recently reported that $Ni_{1-x}Mn_xO$ (x = 1, 3, 5, and 7%) nanoparticles were effectively produced at room temperature utilizing a wet chemical precipitation process with polyethylene glycol as a capping agent [20]. According to the literature, only a few researchers have attempted to investigate the magnetic and supercapacitor characteristics of Mn-doped NiO.

An effort has been completed to resolve the discrepancies between the magnetic and electrochemical properties through this scientific investigation. In this research, pristine and Mn-doped NiO NPs were amalgamated via precipitation method, and the influence of pristine and Mn-doped levels such $Ni_{0.2}O$, $Ni_{0.18}Mn_{0.02}O$, $Ni_{0.16}Mn_{0.04}O$, and $Ni_{0.14}Mn_{0.06}O$ on energy bandgap, magnetic, and electrochemical stability were systematically examined. The produced ($Ni_{0.18}Mn_{0.02}O$) Nano spheres shown superior electrochemical capabilities, as evidenced by their high specific capacitance value of 319 F/g when compared to other dopant samples, according to these data.

2 Experimental details

2.1 Materials requirement

Analytic grade chemicals are used in this scheme. Nickel nitrate hexahydrate [$Ni(NO_3)_2.6H_2O$] is the most important precursor, followed by citric acid, manganese nitrate hexahydrate [$Mn(NO_3)_2.6H_2O$], citric acid [$C_6H_8O_7$], and sodium hydroxide [NaOH], all of which can be purchased at Sigma Aldrich. All sample preparation and dilutions were prepared with Dw (distilled water).

2.2 Synthesis method

2.2.1 Synthesis of pristine NiO nanoparticles

In this experiment, 0.2 M of $Ni(NO_3)_2.6H_2O$, and 0.02 M of $C_6H_8O_7$ has been liquefied in Dw (50 mL) with constant stirring for half an hour. Secondly, 0.1 M of NaOH has been mixed in Dw (50 mL). The latter was incorporated into the previously indicated well-mixed solution, and the pH was maintained at 12. A green precipitate formed in the solution after being stirred on a magnetic stirrer at 80 °C for an hour. Acetone was used to wash the yield to eliminate organic/unwanted contaminants and other unreacted compounds. The entire solution has been micro-oven-heated to 100 °C for 6 h. Calcination at temperature (800 °C) for 4 h resulted in the final yield. A fine powder was made by grinding a sample in a mortar and pestle. The late fine powder era was distinguished by the use of several methods for investigating a variety of attributes. [21].

2.2.2 Synthesis of Mn-doped NiO nanoparticles

In this experiment, 0.18 M of $Ni(NO_3)_2.6H_2O$, 0.02 M $Mn(NO_3)_2.6H_2O$, and 0.02 M of $C_6H_8O_7$ has been liquefied in Dw (50 mL) with constant stirring for half an hour. Secondly, 0.1 M of NaOH has been mixed in Dw (50 mL). The latter was added to the aforementioned homogeneous mixed solution, and the pH was kept at 12. Under continuous stirring on a magnetic stirrer for an hour at 80 °C, the resultant solution gradually changed into a green precipitate. The yield has been washed in acetone to remove organic/unwanted impurities and other unreacted substances from the obtained product. The whole solution has been heated at a temperature of 100 °C for 6 h in a micro-oven. The final yield has been calcinated at a temperature (800 °C) for 4 h. All of the samples were crushed in a mortar and pestle to create a fine powder. Different techniques for the research of different qualities were characteristics of the late fine powder. Similarly, we have adopted the same procedure to make Mn (0.04, and 0.06 M) NiO NPs by substituting stoichiometric quantities of $Mn(Ni(NO_3)_2.6H_2O$ and the flow chart is shown below [22].

2.3 Instrumentation details

The crystalline structure of the synthesized NPs were analyzed using the x-ray diffractometer X'Pert Pro Powder model Cu-Kα radiation (= 1.5406 Å) in the scan range with a step size of 0.017. Fourier transform infrared (FT-IR) spectra from a PerkinElmer Spectrum Two model identified the functional group. The surface morphology of the synthesized NPs was examined using SEM on a JEOL—JSM 5610LV model. The composition of elements such as Ni, Mn, and O were evaluated using EDS. Transmission electron microscope (TEM, model JEOL 3010) has been used to calculate the average particle size of prepared nanoparticles in-depth range. Ultraviolet–Visible (UV–Vis) spectroscopy (Shimadzu-3600 spectrophotometer) has been used to study optical properties such as bandgap. A Vibrating Sample Magnetometer (VSM, model 7410) has been used to study the magnetic behavior of various particles.

2.4 Electrochemical performance

The electrochemical analyzer was used to test the cyclic voltammetry of pristine NiO and Mn-doped NPs. Platinum foil has been used as a reverse electrode, while Ag–AgCl has been used as a reference electrode. Pristine and Mn-doped NiO NPs has been used as working electrodes in three-electrode systems. As an electrolyte, all tests are performed in a 2 M aqueous solution of Na_2SO_4. The electrochemical behavior was assessed using CV, within the + 0.0 to 0.6 V vs Ag–AgCl potential range at 10–100 mV/s scan rate on the versa PARSTAT-MC Series, Princeton Useful Research electrochemical research instruments.

3 Results and discussion

3.1 Structural analysis

Figure 1, demonstrations the XRD peaks of pristine and Mn-doped NiO at different levels (0.02, 0.04, and 0.06 M). The standard peaks of pristine NPs are situated at an angle of 2-Theta (θ) = 37.16°, 43.21°, 62.34°, 75.19°, and 79.24°, and resemble to the planes such as (111), (200), (220), (311), and (222), respectively. Using standard JCPDS card 73-1523, all crystallography peaks are identified and are considered
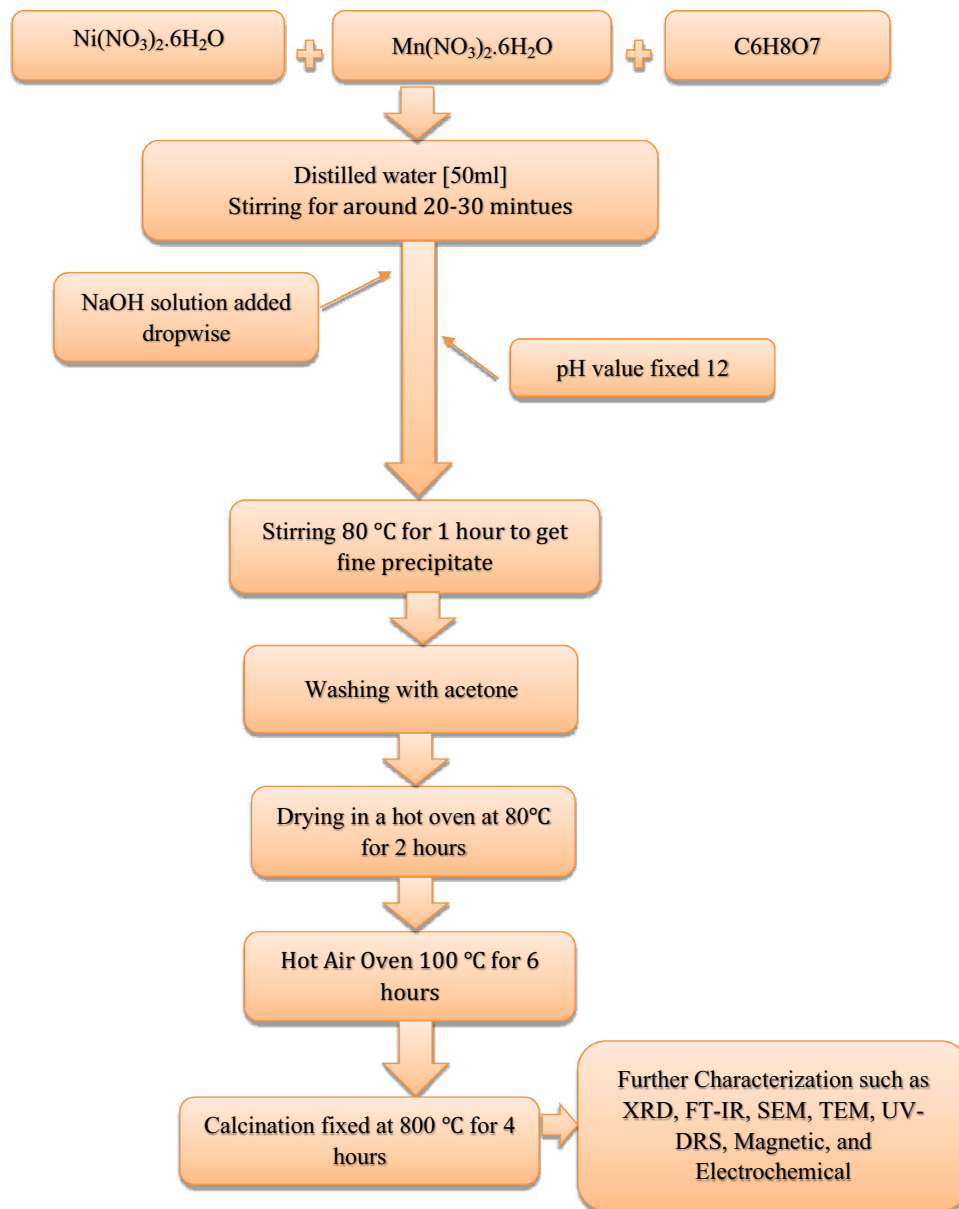
Flow chart for the synthesis of pristine and Mn-doped NiO NPs

to be in the face-centered cubic phase. However, no manganese oxide (MnO) peaks were found up to 0.04 M, indicating that these phases are pure doped NPs with this manufactured design. Additionally, a second phase is seen with higher doping levels (0.06 M). The new phase is associated with MnO NPs that have the JCPDS card 07-0230. Due to the second phase, some of the Mn^{2+} ions are isolated at higher doping levels, i.e., beyond the solubility limit. Generally, the intensity of the XRD peaks reduces significantly with the increase in doping concentrations.

Due to the lattice exaggeration which results from a loss of crystallinity of the material. The strain is developed due to the doping of Mn^{2+} ions in NiO crystal lattice. So, it results from the breaking of crystal symmetry due to the variation of lattice periodicity. Due to the small crystallite size, the peaks become broad and short as compared to pristine NiO NPs. The basic structure of NiO NPs, however, stays the same as in the cubic phase, indicating that Mn^{2+} ions enter the lattice site as substitutional ions, replacing Ni^{2+} ions rather than forming void spaces.

Gopinadhan et al., found a similar outcome reported somewhere else [23]. The average crystallite size of pristine and Mn-doped NiO were estimated to be 28.06, 22.53, 21.02, and 17.31 nm, respectively. Doping Mn^{2+} levels that alter the size of the crystallites in pristine material has produced an intriguing outcome. Based on the outcome, the doped NiO samples occur to have smaller crystallite size than the pristine NiO samples.

The average crystallite size of pristine and Mn-doped NiO NPs was calculated using the Debye-Scherer equation [24–26].

$$D = \frac{k\lambda}{\beta\cos\theta}. \qquad (1)$$

By using the relation of micro-strain (ε) [20, 27].

$$\varepsilon = \frac{\beta\cos\theta}{4}. \qquad (2)$$

The dislocation density was computed using the following relation [28, 29].

$$\delta = \frac{1}{D^2}. \qquad (3)$$

The lattice parameters ($a = b = c$) were computed using the following relation [2].

$$d = \frac{a}{\sqrt{h^2 + k^2 + l^2}}. \qquad (4)$$

The following formula was used to calculate the unit-cell volume [2].

$$V = a^3, \qquad (5)$$

where D = crystallite size of the particle, $k = 0.91$ is treated as a constant number, $\lambda = 0.15405$ nm wavelength Cu-Kα, β = FWHM, θ = Bragg's angle, and a = lattice parameter. The microstructural parameter is framed in Table 1.

Debye Scherrer's formulation simply estimates the size of the crystallites; it is unable to tell us anything about the intrinsic strain caused by peak broadening. Williamson-Hall (W-H) method was used to compute the mean crystallite size and lattice strain utilizing the relation, which makes it more appropriate for this purpose [28, 30].

$$\beta\cos\theta = \frac{k\lambda}{D\cos\theta} + 4\varepsilon\sin\theta. \qquad (6)$$

The equation for the uniform deformation model, which takes into consideration the crystals' isotropic nature, is represented as a straight line. As shown in Fig. 2, the graph for the examined products is drawn between $4 \times \sin\theta$ along the x-axis and $\cos\theta$ along the y-axis. This plotted straight line continues to be accurately fitted and matches all of the values. As a result, the intercept determines the average crystallite size, and the linear slope determines the intrinsic strain value. Table 1 and Fig. 2 show that the average crystallite size for pristine NiO is 27 nm and drops as low as 22 nm for Mn-doped NiO NPs.

3.2 FT-IR spectroscopy

FT-IR analysis is a method to get evidence about chemical bonding in a material. Figure 3, depicts the absorption peaks of all the products which show a hump peaks and weak positions such as 3428 cm^{-1}, 2925 cm^{-1}, 1641 cm^{-1}, 1444 cm^{-1}, 868 cm^{-1}, 525 cm^{-1}, and 446 cm^{-1}. The two peaks are found to be at 1641 cm^{-1} and 3428 cm^{-1} which confirms the bending vibrations of water (H–O–H) molecules and hydroxyl (O–H) stretching molecules. The peak at 2925 cm^{-1} is contributed as C–H_2 molecules which is due to the stretching vibration mode [31–34]. However, the standard characteristic peak at 1444 cm^{-1} leads to the stretching vibration of N–O molecules. The peak at 868 cm^{-1} is attributed to the NaOH molecules [30]. The bending vibrations mode of Ni–O–Mn, which is also clearly visible in the XRD measurements, is responsible for the major absorption peak at 525 cm^{-1}. The stretching mode of the Ni–O
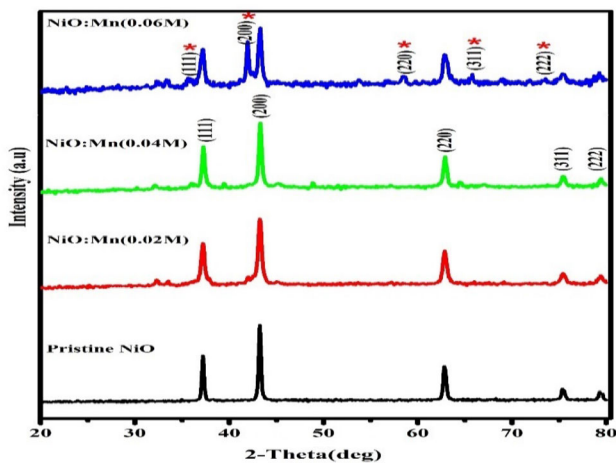

Fig. 1 XRD design of pristine and Mn-doped NiO NPs

(nickel, oxygen) group is responsible for the intermediate peak at 466 cm^{-1} [20].

3.3 UV–Visible absorption

The absorbance spectra of pristine NiO and Mn-doped NiO NPs are analyzed using UV–Visible diffuse reflectance spectroscopy (UV-DRS). Optical absorption spectra of pristine NiO and Mn-doped NiO NPs at various levels such as 0.02, 0.04, 0.06 M in-between the range of 200–800 nm are shown in Fig. 4a, b. It is experimentally identifying that the optical absorption reductions from 270 to 240 nm and it shows decreasing wavelength. The absorption range of pristine NiO NPs is shrinking as a result of Mn^{2+} doping at various concentrations, which could be attributed to differences in photon scattering levels caused by defects formed during doping.

The bandgap of pristine NiO and Mn-doped NiO NPs determined by using Eq. 7 [36, 37].

$$\alpha = \frac{A(h\upsilon - E_g)^{1/2}}{h\upsilon},\tag{7}$$

where α is the "absorption coefficient," A is the "proportionality constant," and E_g is the " energy bandgap." The bandgap of the NiO and Mn-doping NiO was deliberate by plotting of $[F(R)h\upsilon]^2$ versus energy ($h\upsilon$) are shown in Fig. 4c, d. The predictable E_g values of the products are 3.01, 3.25, 3.42, and 3.51 eV, respectively. When Mn (0.02, 0.04, 0.06 M) is doped on NiO NPs, the E_g increases with increasing doping levels, which may be owing to optimum doping levels in the crystal matrix. UV–Visible spectra demonstrate pristine NiO NPs have semiconductor character, where they are acquired from
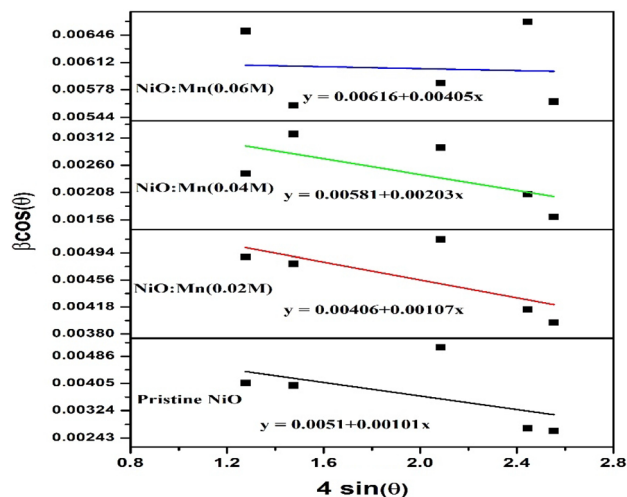

Fig. 2 W-H plot measurement of pristine and Mn-doped NiO NPs

direct bandgap values that vary depending on size and doping materials. The quantum confinement effect is responsible for the increase in $Ni_{1-x}Mn_xO$ energy bandgap values with decreasing crystallite size [35].

3.4 Surface morphology

3.4.1 SEM/EDX analysis

The surface morphology of pristine and Mn-doped NiO with a concentration of 0.06 M is shown in Fig. 5a–d. The SEM analysis reveals that the particles are spherical in shape and formed agglomeration in both samples. During the synthesis, several factors affect thermal influence, hydrogen bonding, chemical bonding, intrinsic crystal defects, and weak forces with high agglomeration in nanoparticles. Figure 5e,

Table 1 The structural parameters of pristine and Mn-doped NiO NPs

| Materials	Debye Scherrer method		W-H method		Dislocation density $(\delta) \times 10^{15}$ L/m^2	Lattice parameter $(a = b = c)$	Cell volume $V = a^3$	E_g (eV)
	Average D (nm)	Micro-strain $\times 10^3 (\varepsilon)$	Average D (nm)	Lattice strain				
Pristine NiO	28	0.9452	27	0.00101	1.2700	4.1831	73.19	3.01
NiO: Mn(0.02 M)	23	1.6880	26	0.00107	1.9700	4.1811	73.09	3.25
NiO: Mn(0.04 M)	21	1.8895	24	0.02036	2.2632	4.1802	73.04	3.42
NiO: Mn(0.06 M)	17	1.9656	22	0.04054	3.3373	4.1775	72.90	3.51
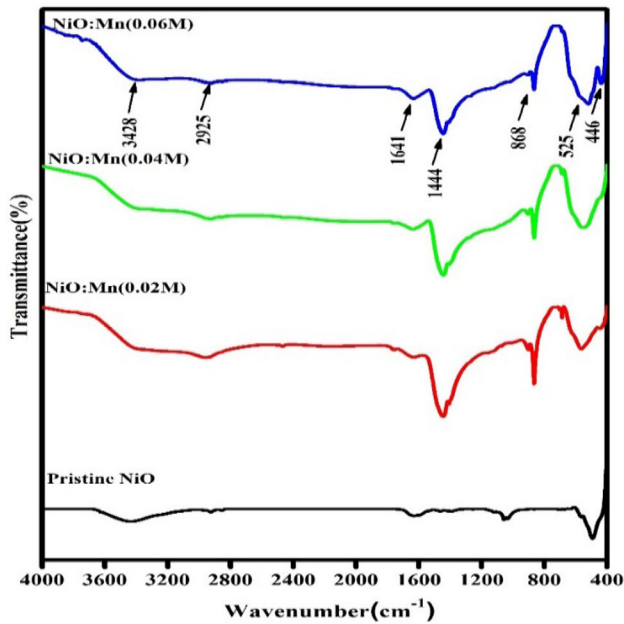
Fig. 3 FT-IR spectra of pristine and Mn-doped NiO NPs

f shows EDX analysis of pristine and Mn-doped NiO NPs. The spectrum of 0.06 M of the Mn-doped sample demonstrates the addition of Mn ions in the reaction, indicating that Mn is perfectively induced into the NiO position. It demonstrates sample contains a Mn ion, which is also visible in the XRD result.

3.4.2 TEM/SAED

The surface morphology such as the size and shape of the pristine and doped samples were furthermore analyzed through TEM with SAED pattern measurement. Figure 6a–f shows TEM images of pristine and Mn-doped (0.06 M) samples of NiO NPs. The TEM images were revealed with different nanometers, which experimentally catch that the shape of the particles is spherical, and is also well-known in SEM analysis. The SAED pattern image of pristine pristine and Mn-doped (0.06 M) samples of NiO NPs exhibits bright crystalline spots pattern belonging to NiO peaks whereas the highly bright ring structures belong to Mn-doping NiO samples as shown in Fig. 6e, f. The average particle size of the pristine and Mn-doped NiO NPs, respectively, is 32 and 23 nm, as shown in Fig. 6g, h, which is in good agreement with the XRD data.

3.5 Magnetic analysis (VSM)

Hysteresis curves of pristine NiO and Mn-doped NiO NPs measured at RT (room temperature) are shown in Fig. 7a–d. Superparamagnetic behavior is observed in Mn^{2+}-doped samples, but weak ferromagnetic behavior is observed in pristine NiO NPs. The weak ferromagnetic changes into superparamagnetic behavior. The cause of the superparamagnetic activities in NiO nanoparticles can be ascribed due to the surface effects, finite-size effects and interparticle interactions. These effects are related to a decrease in the number of exchange-coupled spins within nanoparticles and the decreased symmetry of surface atoms due to incomplete compensation between antiferromagnetic sub-lattices. The fraction of surface to total spins in antiferromagnetic nanoparticles depends on the crystallite size, coercivity and magnetic moment should vary with crystallite size. Besides, the shape of the hysteresis curve squareness will be significantly affected by the surface magnetic anisotropy [20, 37]. Table 2, shows the magnetization remanent (M_r), saturation magnetization (M_s), coercivity (H_c), and squareness ratio (SQR) of pristine and Mn-doped NiO NPs. The pristine NiO shows weak ferromagnetic behavior with M_s is 0.905 emu/g and Mn-doped NiO NPs illustration superparamagnetic behavior with different doping levels (0.02, 0.04, and 0.06 M). The Ms values observed for Mn-doped NiO NPs are 0.32 emu/g, 0.36 emu/g, and 0.37 emu/g, respectively. It is clearly seen that the magnetic moment of the doped (Mn^{2+}) samples are higher in contrast to pristine NiO NPs. Therefore, the addition of Mn ions doping can increase the net magnetization. The 0.02 M% of Mn^{2+}-doped NiO NPs show a small Hc field due to less aspect ratio, whereas, 0.04 M% and 0.06 M% show a higher H_c field, respectively, depending upon the aspect ratio. Ni^{2+} (0.69 Å) and Mn^{2+} (0.66 Å) have an almost similar ionic radius and are chemically equivalent to octahedral. The Mn^+ ions is easily predictable to inhabit the Ni^+ ions site in the NiO medium. The lackness of a defect in the second phase within the range of 0.06 M% of Mn^{2+}-doped NiO NPs is well evident with XRD. The dimension of the particles is diminished to the nanoscale size. The antiferromagnetic materials of NiO can demonstrate with various magnetic properties like spin-glass behavior (crystallite size $D \leq 10$ nm), ferromagnetism ($D \leq 20$ nm), and Superparamagnetism ($D \leq 32$ nm) [38]. The
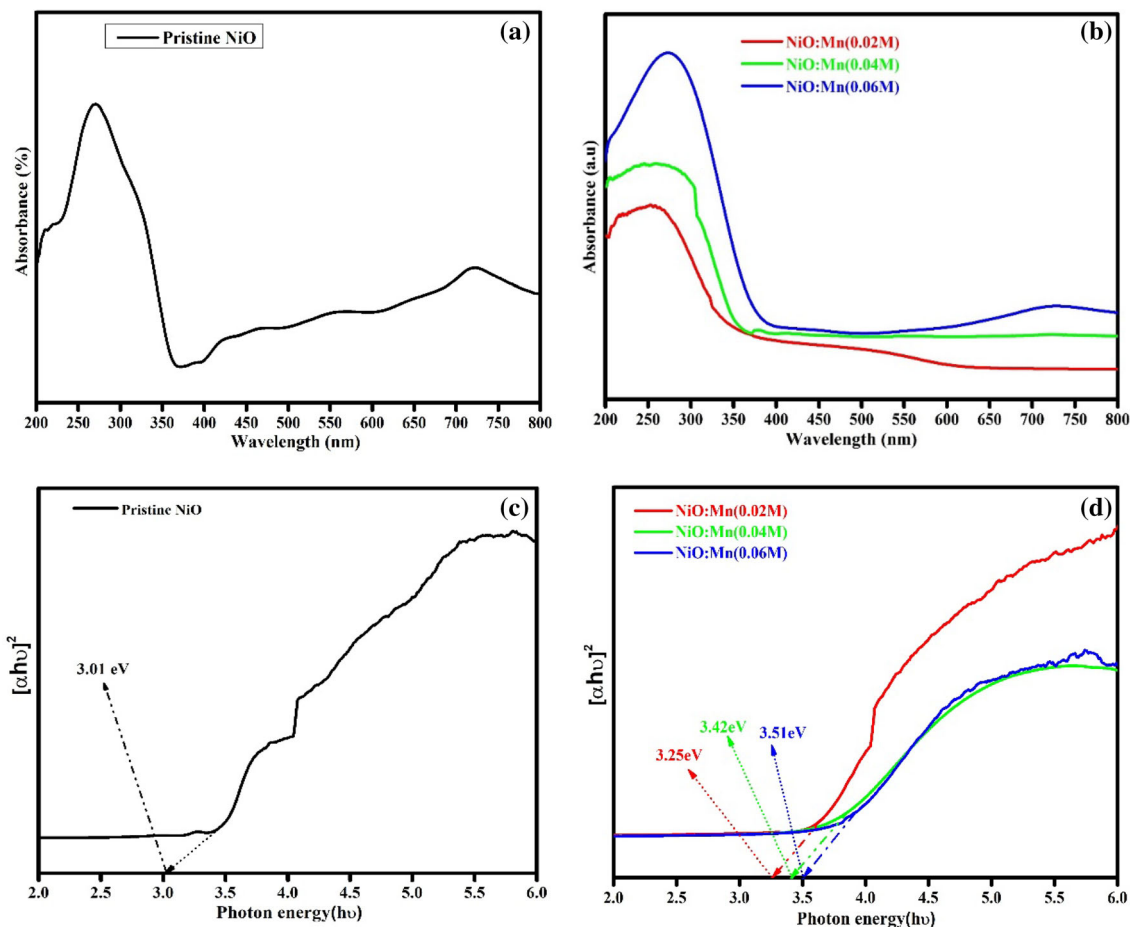
Fig. 4 **a**, **b** Uv absorption and **c**, **d** energy bandgap of pristine and Mn-doped NiO NPs

magnetic properties of Mn^{2+}-doped NiO NPs have been studied and found to be dependent on the following factors. (i) The finite size occurs as a result of the surface spins integrating, (ii) Mn^{2+} contaminant levels, and (iii) Mn^{2+} ions occupy the Ni^{2+} site. It has been investigated that these possibilities were confirmed in our samples. The magnetization at lower fields confirmed the abrupt rise of the superparamagnetic nature of these particles. The H_c field is the inverse of the magnetic field that reduces the net magnetization to 0 (zero). Table 2, shows that 0.02 M Mn^{2+}-doped NPs have a reasonably small H_c field as associated to that of the pristine NiO and other two dopant materials. The decrease in the Hc field can be shown by the effect of Mn-Ni bilayers. Mr is one more quantity, it can be clarified as the residual part of the magnetic moment after realizing the magnetic field. The minimum value of M_r represents magnetically pristine materials [39]. In our observations, a low value of M_r is reported for Mn^{2+}-doped samples,

which is extremely attractive for data storage applications such as RAM and ROM.

3.6 Electrochemical studies

The CV curves of pristine NiO and Mn-doped NiO electrodes at scan rates of 10–100 mV/s are displayed in Fig. 8a–d. Because of the anodic and cathodic peaks in Fig. 8, it can be concluded that the capacitance behavior is entirely distinct from that of an electric double-layer capacitor (EDLC). The samples exhibit pseudocapacitive behavior, evidenced by the existence of redox peaks, which favors reversible electrochemical reactions. Pseudocapacitance has made significant strides thanks to high energy transmission through the faradaic technique, which offers 10, 20, up to 100 times higher capacitance than EDLC nature [2]. A reversible chemical response could be produced by the insertion and de-insertion of Na_2SO_4 into the NiO framework.
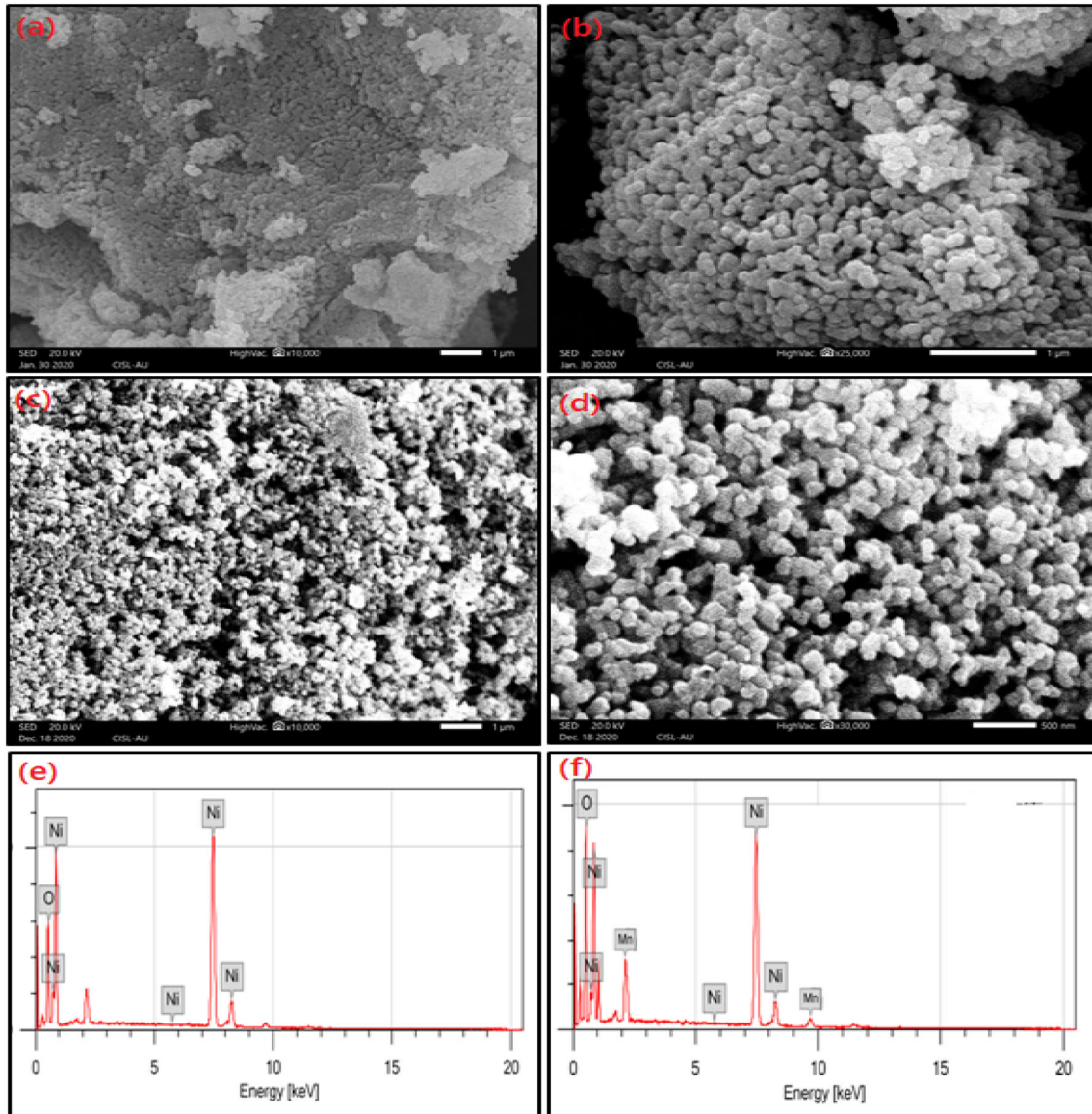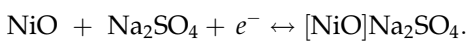
Fig. 5 **a**–**d** SEM image, and **e**, **f** EDX spectra of pristine and Mn-doped (0.06 M) NiO NPs

$$NiO \; + \; Na_2SO_4 + e^- \leftrightarrow [NiO]Na_2SO_4.$$

By using formula, the specific capacitance (Cs) measurements of the pristine NiO and Mn-doped NiO NPs of all the electrodes were calculated [34, 40].

$$Cs = \frac{1}{m(Vf - Vi)} \int_{Vi}^{Vf} I(V)dV, \tag{8}$$

Or

$$Cs = \frac{Q}{m\Delta V}. \tag{9}$$

Here, Q = cathodic and anodic charges, ΔV = potential window, and m = mass (mg) of the electrode's.

Table 3 and Fig. 9 show the specific capacitance of various electrodes obtained using the above equation. It has been investigated that the pristine NiO electrode confirmed the specific capacitance of 555, to 55 F/g, corresponding to different scan rates of 10, to 100 mV/s. However, the doped Mn^{2+}(0.06 M) NiO electrode shows various specific capacitance at 194, to 19 F/g corresponds to different scan rates of 10, to 100 mV/s, respectively. It has been investigated that the Cs is very great measured at a low scan rate.
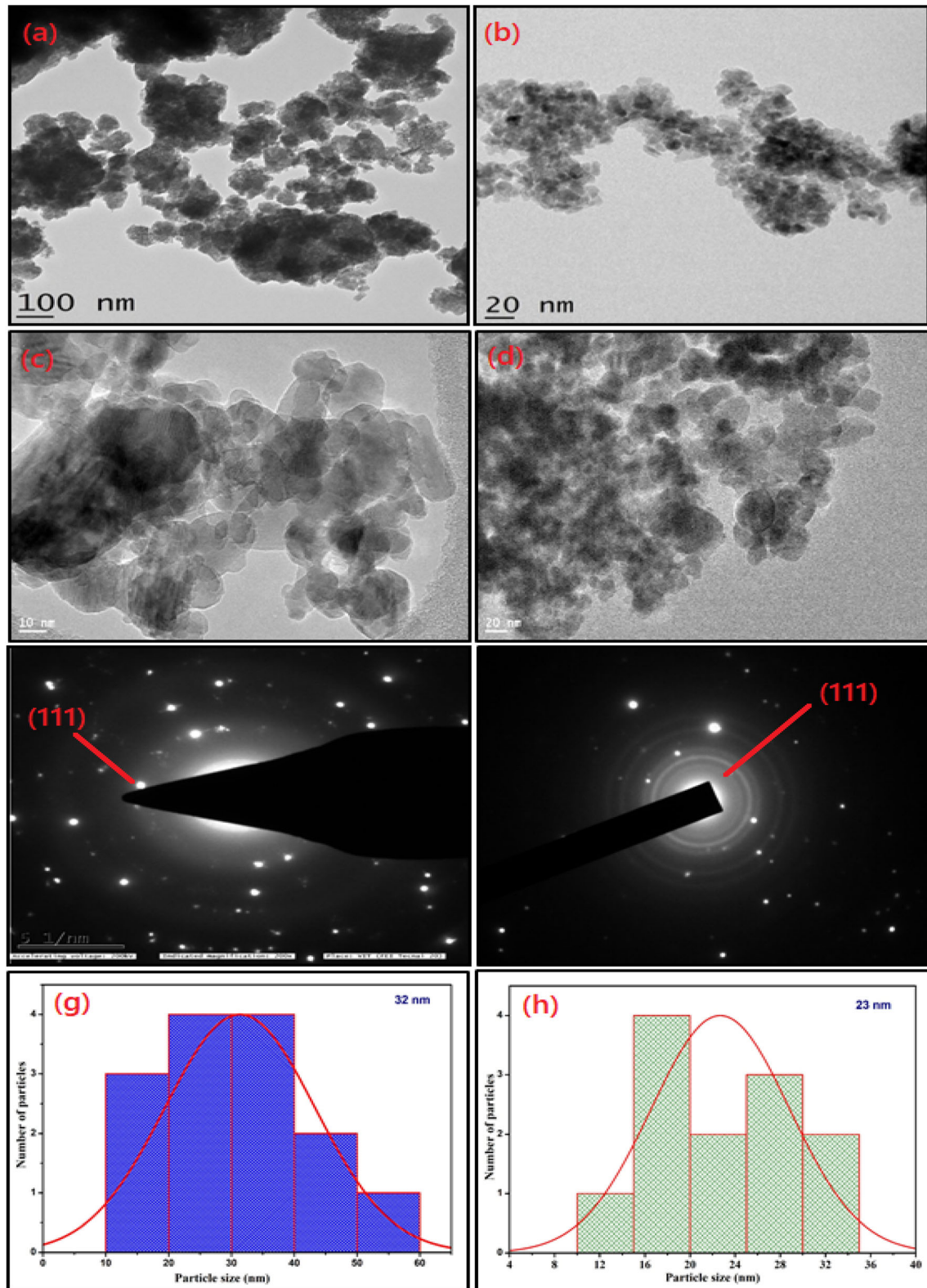
Fig. 6 **a**–**d** TEM images, **e**, **f** SEAD spectra, **g**, **h** particle size distribution of pristine and Mn-doped (0.06 M) NiO NPs
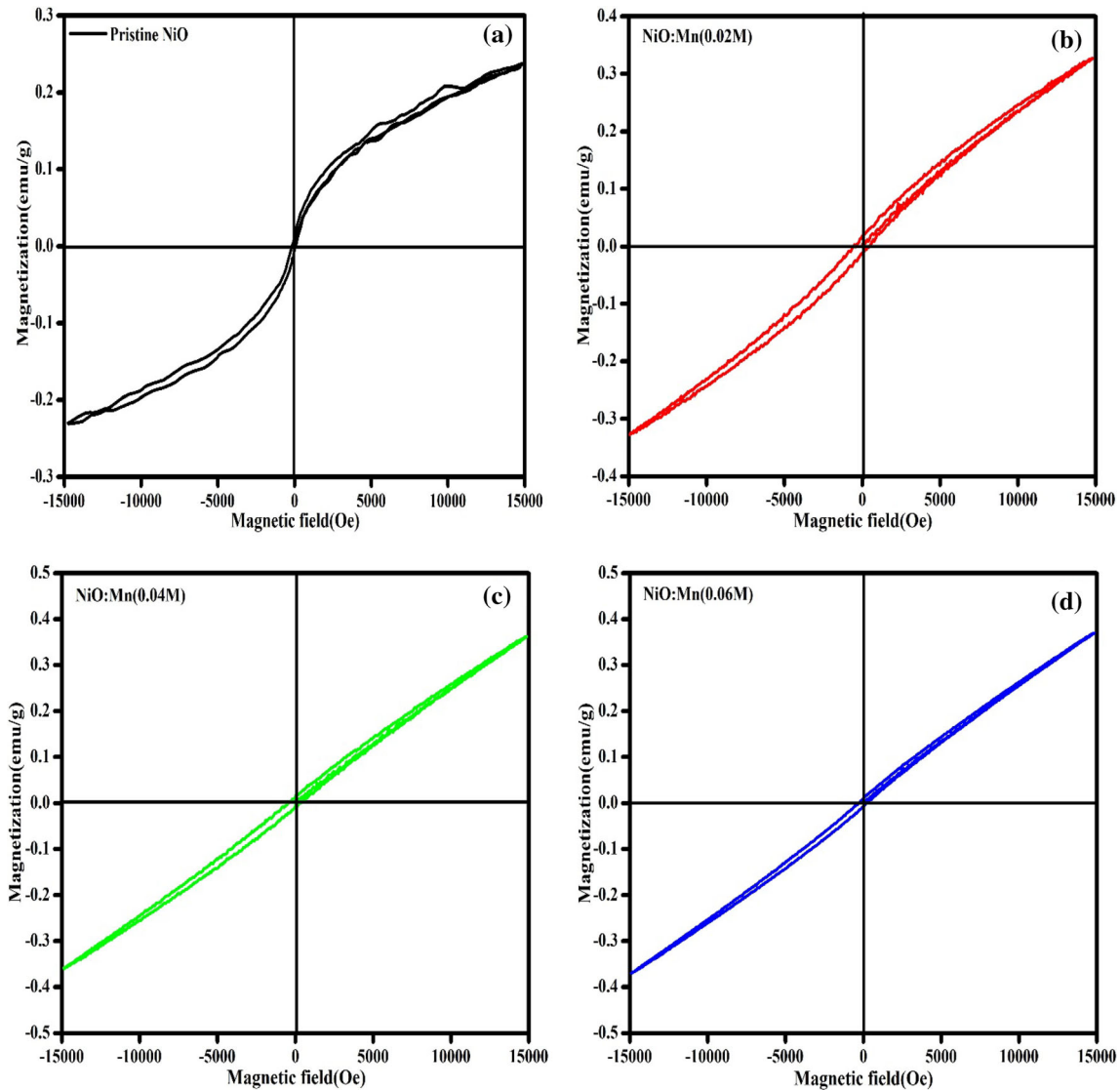
Fig. 7 Magnetic hysteresis of pristine and Mn-doped NiO NPs

Table 2 Magnetic parameters of pristine and Mn-doped NiO NPs

Materials	Hysteresis parameters (VSM)			$M_r/M_s = SQR$
	H_c (Oe)	M_s (emu/g)	$M_r \times 10^{-3}$ emu/g	$SQR \times 10^{-3}$
Pristine NiO	140	0.23	0.90	3.91
NiO:Mn(0.02 M)	10.26	0.32	0.15	0.47
NiO:Mn(0.04 M)	40.78	0.36	0.11	0.30
NiO:Mn(0.06 M)	89.87	0.37	0.08	0.22

Apart from that high Cs measured at a low scan rate is due to the small faradaic reaction. Both the inside and outside surfaces are trustworthy for the calibration of particular capacitance at a low scan rate. In contrast, the ionic dispersion from the outside region occurs at high scan rates [41]. Our results confirmed that with a scan rate of 100 mV/s, the Cs keeps the charge at 55 F/g and 19 F/g. The specific capacitance values decreased after Mn doping, which could be attributable to the electrochemically inactive
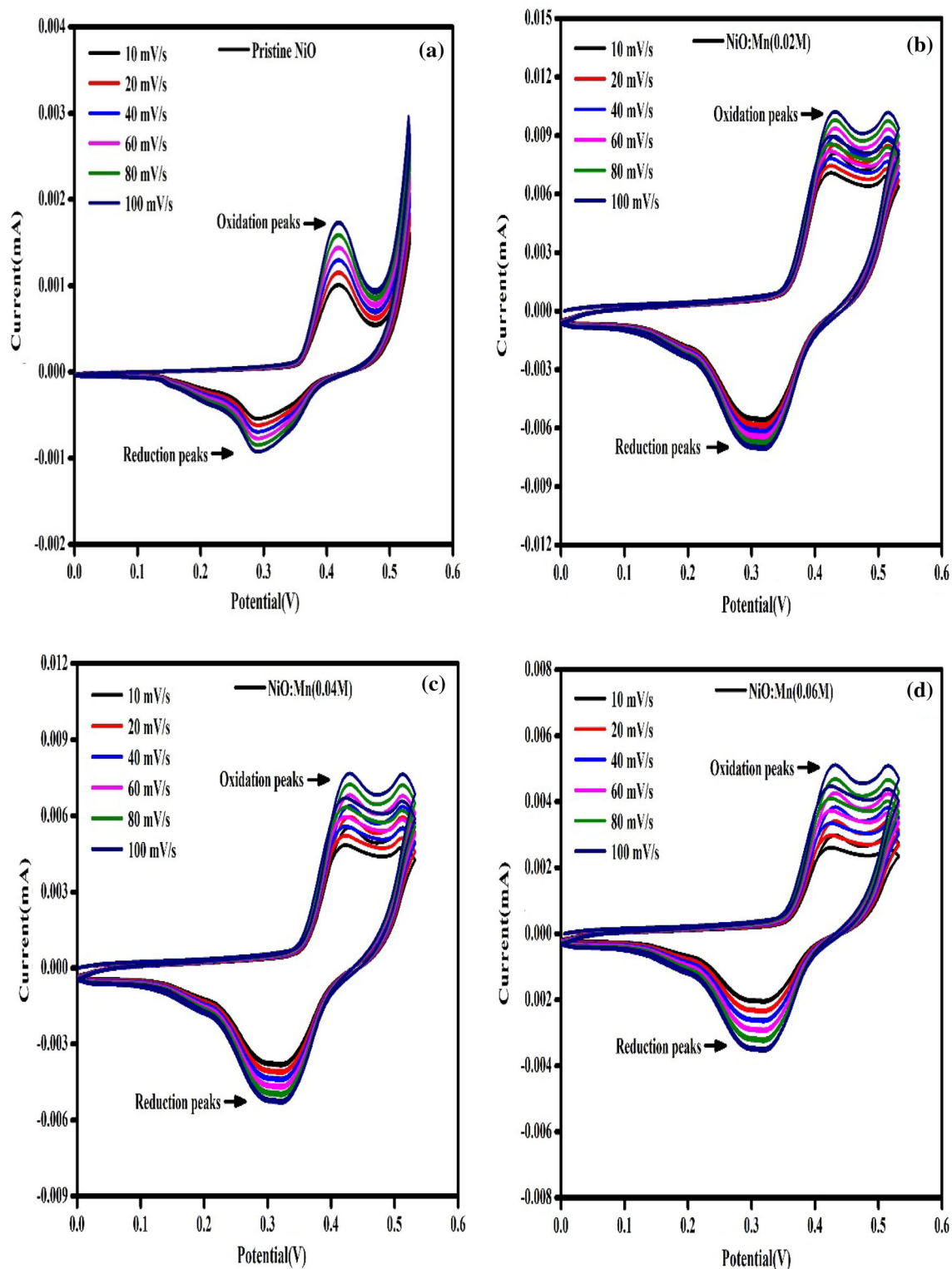
Fig. 8 a–d CV curves of pristine and Mn-doped NiO electrodes

materials [38]. For insight into the synthesized materials' super capacitance behavior. The Scan rate versus the capacitance value was graphed. It can be seen from the graph that as the scan rate is increased, the specific capacitance decreases; this is because of the ion exchange mechanism in the reaction time.

Table 3 Specific capacitance of pristine and Mn-doped NiO electrodes

Scan rate (mV/s)	10	20	40	60	80	100
Samples	Specific capacitance (F/g)					
Pristine NiO	555	277	138	92	69	55
Mn(0.02 M):NiO	319	160	80	53	40	32
Mn(0.04 M):NiO	236	118	59	39	29	24
Mn(0.06 M):NiO	194	97	49	32	23	19

Ions can diffuse into the NiO electrode when the scan rate is low. If it is too high, there is not enough time for ions to intercalate with the electrode. Discharge curves reveal that the low IR drop is due to the poor interaction with the electrode, which reduces the value of specific capacitance [38, 42]. NiO nanoparticles appear to be a promising electrode material for use in supercapacitors.

4 Conclusion

In this study, the chemical precipitation method was used to synthesize the pristine and Mn-doped NiO NPs. The complete structural stability of the synthesized materials is depicted by the FT-IR analysis. The insertion of Mn ions into the NiO lattice causes the crystallite size of the pristine samples to be decreased with a little shift towards the lower diffraction angles and the decrease in crystallite size and the optical bandgap are inversely correlated. Pristine NiO NPs VSM curve demonstrated weak ferromagnetic characteristics. However, when Mn^{2+} ions are doped, the weak ferromagnetic property transforms into
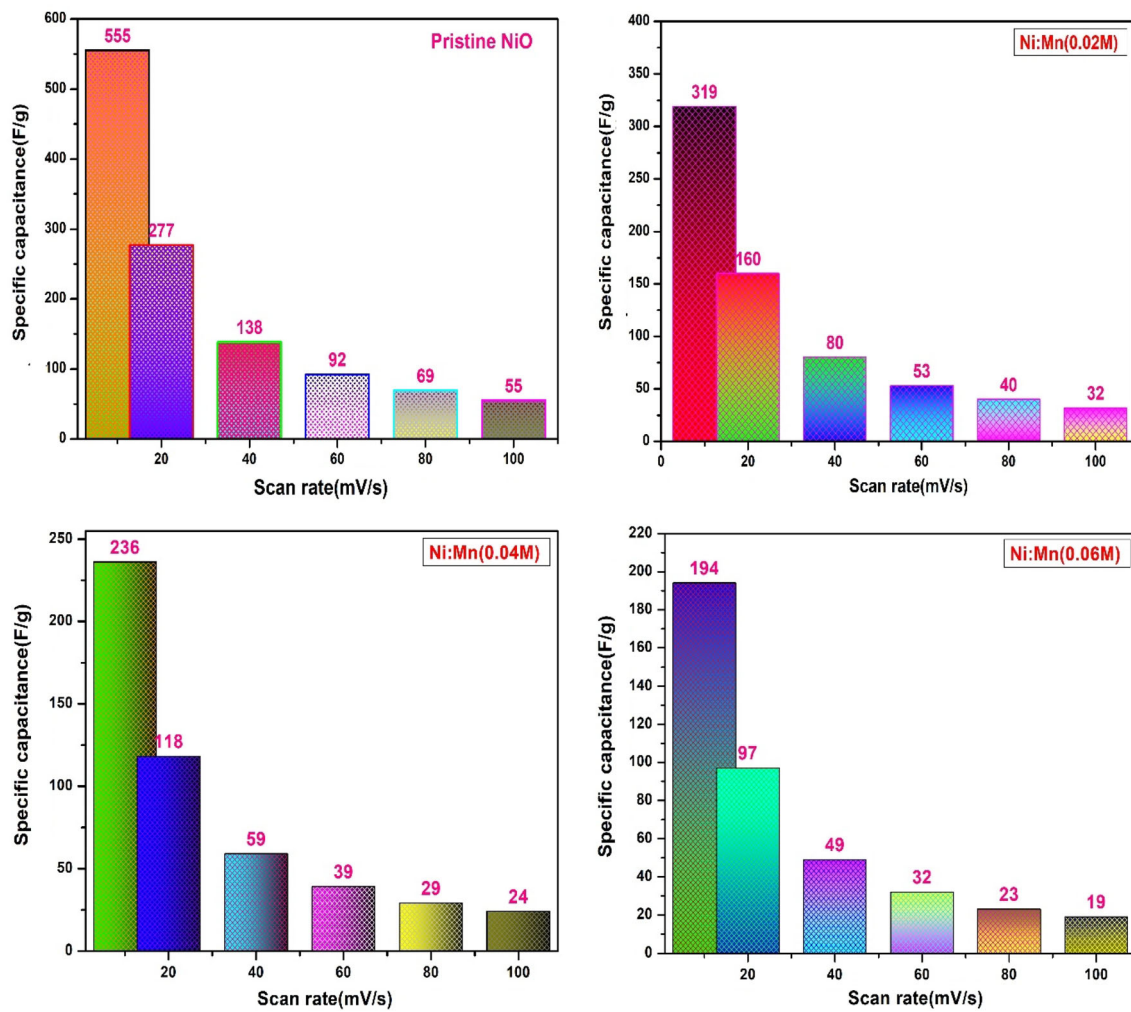

Fig. 9 Specific capacitance values of pristine and Mn-doped NiO electrodes at various scan rates

superparamagnetic behavior. For data storage applications, high inclusion of doped (Mn^{2+} ions) NiO NPs is very desirable. Due to the inclusion of Mn^{2+} ions, the Cs values were reduced from 555 to 194 F/g. Pristine NiO NPs elucidate supreme Cs of 555 F/g at 10 mV/s.

Acknowledgments

Author contributions

SS contributed to supervision, and visualization; NAM contributed to methodology, validation, conceptualization, formal analysis, visualization, writing of the original draft, and writing, reviewing, & editing of the manuscript; MAD, MDR, KMB, BAR, and ZA contributed to reviewing, & editing of the manuscript.

Data availability

All the data are generated or analyzed during this study are included in this published article.

Declarations

Conflict of interest The authors declare that they have no competing financial interests or personal relationships that could have appeared to influence the work reported in this report.

References

1. G. Wang, L. Zhang, J. Zhang, A review of electrode materials for electrochemical supercapacitors. Chem. Soc. Rev. **41**(2), 797–828 (2012)

2. N.A. Mala, M.A. Dar, S. Sivakumar, S. Husain, K.M. Batoo, Enhanced electrochemical properties of zinc and manganese co-doped NiO nanostructures for its high-performance supercapacitor applications. Inorg. Chem. Commun. **142**, 109661 (2022)

3. K. Sathishkumar, N. Shanmugam, N. Kannadasan, S. Cholan, G. Viruthagiri, Influence of Zn^{2+} ions incorporation on the magnetic and pseudo capacitance behaviors of NiO nanoparticles. Mater. Sci. Semicond. Process. **27**, 846–853 (2014)

4. S. Sivakumar, N.A. Mala, K.M. Batoo, E.H. Raslan, Efficient, highly stable Zn^{2+} doped NiO nanoparticles with enhanced magnetic and supercapacitor applications. Mater. Technol. **37**(10), 1375–1387 (2022)

5. S. Thota, J.H. Shim, M.S. Seehra, Size-dependent shifts of the Néel temperature and optical band-gap in NiO nanoparticles. J. Appl. Phys. **114**(21), 214307 (2013)

6. Z. Li, L. Wei, Y. Liu, Y. Su, X. Dong, Y. Zhang, Facile synthesis of single-crystalline mesoporous NiO nanosheets as high-performance anode materials for Li-ion batteries. J. Mater. Sci.: Mater. Electron. **28**(18), 13853–13860 (2017)

7. F.I. Dar, K.R. Moonoosawmy, M. Es-Souni, Morphology and property control of NiO nanostructures for supercapacitor applications. Nanoscale Res. Lett. **8**(1), 1–7 (2013)

8. I. Hotovy, J. Huran, L. Spiess, S. Hascik, V. Rehacek, Preparation of nickel oxide thin films for gas sensors applications. Sens. Actuators B Chem. **57**(1–3), 147–152 (1999)

9. C. Nie, W. Zeng, Y. Li, The 3D crystal morphologies of NiO gas sensor and constantly improved sensing properties to ethanol. J. Mater. Sci.: Mater. Electron. **30**(2), 1794–1802 (2019)

10. M. Martini, G.E.D.S. Brito, M.C.D.A. Fantini, A.F. Craievich, A. Gorenstein, Electrochromic properties of NiO-based thin films prepared by sol–gel and dip coating. Electrochim. Acta **46**(13–14), 2275–2279 (2001)

11. X.Y. Liu, Y.Q. Zhang, X.H. Xia, S.J. Shi, Y. Lu, X.L. Wang et al., Self-assembled porous $NiCo_2O_4$ hetero-structure array for electrochemical capacitor. J. Power Sources **239**, 157–163 (2013)

12. H. Zhu, D.C. Rosenfeld, M. Harb, D.H. Anjum, M.N. Hedhili, S. Ould-Chikh, J.M. Basset, Ni–M–O (M= Sn, Ti, W) catalysts prepared by a dry mixing method for oxidative dehydrogenation of ethane. ACS Catal. **6**(5), 2852–2866 (2016)

13. S. Sankar, S.K. Sharma, N. An, H. Lee, D.Y. Kim, Y.B. Im et al., Photocatalytic properties of Mn-doped NiO spherical nanoparticles synthesized from sol-gel method. Optik **127**(22), 10727–10734 (2016)

14. B. Ebin, Simple preparation of Ni and NiO nanoparticles using raffinate solution originated from spent NiMH battery recycling. J. Inorg. Organomet. Polym Mater. **28**(6), 2554–2563 (2018)

15. D. Hong, W. Yan, Q. Liu, T. Yao, Z. Sun, S. Wei, Structures and magnetic properties of Mn-doped NiO thin films. J. Phys. D Appl. Phys. **47**(29), 295001 (2014)

16. M.J. Kartha, B.A. Reshi, P.S. Walke, D. Dastan, Morphological study of thin films: simulation and experimental

insights using horizontal visibility graph. Ceram. Int. **48**(4), 5066–5074 (2022)

17. Z.Y. Wang, R.H. Fan, Q.Q. Li, L. Qian, Preparation of NiO nanosheets by hydrothermal method and its electrochemical capacitive properties. Mater. Sci. Forum **848**, 396–400 (2016)

18. B.A. Reshi, S. Kumar, A. Misra, R. Varma, Multivariable study on growth of diamond on diamond substrates by microwave plasma chemical vapour deposition. Mater. Res. Express **6**(4), 046407 (2019)

19. K. Anandan, V. Rajendran, Effects of Mn on the magnetic and optical properties and photocatalytic activities of NiO nanoparticles synthesized via the simple precipitation process. Mater. Sci. Eng. B **199**, 48–56 (2015)

20. C. Thangamani, P. Vijaya Kumar, K. Gurushankar, K. Pushpanathan, Structural and size dependence magnetic properties of Mn-doped NiO nanoparticles prepared by wet chemical method. J. Mater. Sci.: Mater. Electron. **31**(14), 11101–11112 (2020)

21. N.A. Mala, M.A. Dar, S. Sivakumar, K.S. Bhat, G.N. Sinha, K.M. Batoo, Electrochemical supremacy of cobalt-doped nickel oxide and its supercapacitor applications with its mesoporous morphology. J. Mater. Sci.: Mater. Electron. **33**(14), 11582–11590 (2022)

22. S. Sivakumar, N.A. Mala, Synthesis and characterization of manganese doping on NiO nanoparticles and its supercapacitor applications. Mater. Today: Proc. **49**, 1469–1474 (2022)

23. K. Gopinadhan, S.C. Kashyap, D.K. Pandya, S. Chaudhary, High temperature ferromagnetism in Mn-doped SnO_2 nanocrystalline thin films. J. Appl. Phys. **102**(11), 113513 (2007)

24. M.A. Dar, D. Govindarajan, K.M. Batoo, M. Hadi, G.N. Dar, Photovoltaic and Supercapacitor performance of SnSe nanoparticles prepared through co-precipitation method. Mater. Technol. **37**(10), 1396–1409 (2022)

25. R. Sathish Kumar, S. Johnson Jeyakumar, M. Jothibas, I. Kartharinal Punithavathy, J. Prince Richard, Influence of molar concentration on structural, optical and magnetic properties of NiO nanoparticles. J. Mater. Sci.: Mater. Electron. **28**(20), 15668–15675 (2017)

26. M.A. Dar, D. Govindarajan, G.N. Dar, Comparing the electrochemical performance of bare SnS and Cr-doped sns nanoparticles synthesized through solvothermal method. Phys. Solid State **63**(9), 1343–1350 (2021)

27. M.A. Dar, N.A. Mala, G.N. Dar, S.S. Kumar, D. Govindarajan, Structural, optical, antibacterial analysis of Se NPs synthesized by precipitation method. Adv. Nat. Sci.: Nanosci. Nanotechnol. **11**(4), 045001 (2020)

28. M.A. Dar, D. Govindarajan, G.N. Dar, Facile synthesis of SnS nanostructures with different morphologies for supercapacitor and dye-sensitized solar cell applications. J. Mater. Sci.: Mater. Electron. **32**(15), 20394–20409 (2021)

29. M.A. Dar, M.Y. Bhat, N.A. Mala, H.A. Rather, S. Venkatachalam, N. Srinivasan, Structural, morphological and supercapacitor applications of SnS nanomaterials prepared in three different types of solvents. Mater. Today: Proc. **66**, 1689–1698 (2022)

30. M.A. Dar, D. Govindarajan, K.M. Batoo, C. Siva, Supercapacitor and magnetic properties of Fe doped SnS nanoparticles synthesized through solvothermal method. J. Energy Storage **52**, 105034 (2022)

31. B.J. Rani, G. Ravi, R. Yuvakkumar, S. Ravichandran, F. Ameen, A. Al-Sabri, Efficient, highly stable Zn-doped NiO nanocluster electrocatalysts for electrochemical water splitting applications. J. Sol-Gel. Sci. Technol. **89**(2), 500–510 (2019)

32. N.A. Mala, S. Sivakumar, K.M. Batoo, M. Hadi, Design and fabrication of iron-doped nickel oxide-based flexible electrode for high-performance energy storage applications. Inorg. Chem. Commun. **131**, 108797 (2021)

33. Z. Ahmad, S. Kumar, C.K. Trinh, J.J. Shim, J.S. Lee, Decoupling electrochemical parameters of molecular-level-controlled polypyrrole and graphene oxide nanocomposite. Appl. Surf. Sci. **610**, 155464 (2023)

34. Z. Ahmad, W.B. Kim, S. Kumar, T.H. Yoon, J.J. Shim, J.S. Lee, Redox-active supercapacitor electrode from two-monomer-connected precursor (Pyrrole: Anthraquinonedisulfonic acid: Pyrrole) and sulfonated multi-walled carbon nanotube. Electrochim. Acta **415**, 140243 (2022)

35. B. Govindarajan, R. Palanimuthu, K.M. Manikandan, Influence of Mg doping in magnetic properties of NiO nanoparticles and its electrical applications. J. Mater. Sci.: Mater. Electron. **30**(7), 6519–6527 (2019)

36. S. Sivakumar, N.A. Mala, K.M. Batoo, M.F. Ijaz, Conserved crystal phase and morphology: electrochemical supremacy of copper (Cu) and iron (Fe) dual-doped nickel oxide and its supercapacitor applications. Inorg. Chem. Commun. **134**, 108959 (2021)

37. A. Jafari, S.P. Jahromi, K. Boustani, B.T. Goh, N.M. Huang, Evolution of structural and magnetic properties of nickel oxide nanoparticles: influence of annealing ambient and temperature. J. Magn. Magn. Mater. **469**, 383–390 (2019)

38. G. Bharathy, P. Raji, Room temperature ferromagnetic behavior of Mn doped NiO nanoparticles: a suitable electrode material for supercapacitors. J. Mater. Sci.: Mater. Electron. **28**(23), 17889–17895 (2017)

39. S. Farhadi, Z. Roostaei-Zaniyani, Simple and low-temperature synthesis of NiO nanoparticles through solid-state thermal decomposition of the hexa (ammine) Ni (II)

nitrate,[Ni(NH$_3$)$_6$](NO$_3$)$_2$, complex. Polyhedron **30**(7), 1244–1249 (2011)

40. S.J. Uke, S.P. Mardikar, D.R. Bambole, Y. Kumar, G.N. Chaudhari, Sol-gel citrate synthesized Zn doped MgFe$_2$O$_4$ nanocrystals: a promising supercapacitor electrode material. Mater. Sci. Energy Technol. **3**, 446–455 (2020)

41. S. Kumar, I.A. Mir, Z. Ahmad, K. San Hui, D.A. Dinh, L. Zhu et al., Microflowers of Sn-Co-S derived from ultra-thin nanosheets for supercapacitor applications. J. Energy Storage **49**, 104084 (2022)

42. G. Srikesh, A.S. Nesaraj, Facile preparation and characterization of novel manganese doped nickel oxide based nanostructured electrode materials for application in electrochemical supercapacitors. J. Asian Ceram. Soc. **8**(3), 835–847 (2020)